


## Article

# Optimal Design and Dynamic Analysis of a Spring-Actuated Cam-Linkage Mechanism in a Vacuum Circuit Breaker

Yaw-Hong Kang , Hua-Chih Huang and Bo-Ya Yang

Department of Mechanical Engineering, National Kaohsiung University of Science and Technology, Kaohsiung City 80778, Taiwan

\* Correspondence: yhkang@nku.edu.tw; Tel.: +886-07-3814526

**Abstract:** This study attempted to establish an optimal design and perform dynamic analysis for a spring-actuated cam-linkage composite mechanism in a rated 12 kV, 25 kA vacuum circuit breaker (VCB). The optimal design of the VCB mechanism involves two steps: the first step involves the optimal design of the stiffness of closing springs and the cam profile, based on three-order polynomial motion curve of the follower; the second step involves the optimal design of a four-bar linkage. To minimize the surplus work in the VCB operating mechanism, the overall difference between the general output force and general resistant force of the VCB operating mechanism during the closing operation was adopted as the objective function to be minimized. Furthermore, the differential evolution algorithm with the golden ratio (DE-gr), an efficient and accuracy metaheuristic algorithm, was employed as the optimization method. The dynamic analysis of the optimal operating mechanism was conducted using a MATLAB-coded program and verified by the multibody dynamic software MSC-ADAMS. The dynamic analysis revealed that the optimal design of the VCB mechanism can considerably decrease the average closing velocity of the movable contact and the Hertz stress between the contact surface of the cam and the roller follower.

**Keywords:** vacuum circuit breaker (VCB); cam-linkage composite mechanism; differential evolution (DE); Hertz contact stress



**Citation:** Kang, Y.-H.; Huang, H.-C.; Yang, B.-Y. Optimal Design and Dynamic Analysis of a Spring-Actuated Cam-Linkage Mechanism in a Vacuum Circuit Breaker. *Machines* **2023**, *11*, 150. <https://doi.org/10.3390/machines11020150>

Academic Editors: Loránd Szabó and Feng Chai

Received: 20 November 2022

Revised: 13 January 2023

Accepted: 18 January 2023

Published: 21 January 2023



**Copyright:** © 2023 by the authors. Licensee MDPI, Basel, Switzerland. This article is an open access article distributed under the terms and conditions of the Creative Commons Attribution (CC BY) license (<https://creativecommons.org/licenses/by/4.0/>).

## 1. Introduction

Power circuit breakers (CBs) are the core switches of power systems that prevent accidents by instantly interrupting abnormal currents, such as over current, short circuit, and ground fault current. Therefore, CBs provide safe protection or control mechanisms for electrical equipment. Several different types of power CBs have been developed using air, oil, compressed air, SF<sub>6</sub> gas, and vacuum as interrupting mediums [1]. The vacuum circuit breaker (VCB), which extinguishes the arc in a vacuum interrupter and has favorable features, such as small size, high efficiency and reliability, and easy maintenance; it is often used to interrupt electric current in power transmission lines with voltages ranging from 3.6 to 38 kV [2]. The cam-linkage composite operating mechanisms are extensively employed in conventional VCBs to complete rapid opening and closing actions within several tens of milliseconds [3]. Several studies have attempted designs and/or investigated the dynamics of the operating mechanisms of CBs. Pisano et al. [4,5] experimentally investigated and analyzed the dynamic response of a high-speed cam follower system. Root et al. [6] optimized the design of the operating mechanism of Westinghouse Type R VCBs. An integrated machine program (IMP) was embedded as an analysis routine within an optimization algorithm, which was a pattern-search method coupled with a penalty function of multipliers. Jobes et al. [7] presented type synthesis and optimal dimensional synthesis of a controllable CB. Furthermore, the simulation, kinematic and dynamic analyses of the optimal mechanism were performed and validated using the multibody dynamic software Automated Dynamic Analysis of Mechanical Systems (ADAMS). Ahn et al. [3]

derived a dynamic model for a high-speed CB mechanism with a spring-actuated cam, and experimentally validated the high-speed motion behavior. The model highlighted the effects of friction on the camshaft, and the characteristics and parameters of the friction were analyzed through a nonlinear pendulum experiment and a modified simplex optimization method, respectively. Kim et al. [8] performed an optimal synthesis for a spring-actuated cam with non-constant angular velocities and an optimized cubic-spline follower motion. The dynamic characteristics of the optimal cam and follower were simulated using ADAMS, and the results indicated that the dynamic behaviors of the optimal cam were superior to those of the polynomial cam with constant angular velocity. Chen et al. [9] investigated the dynamics of a spring-type operating mechanism for a gas-insulated CB. The Lagrange equation was applied to derive the dynamic equation for the opening operation, and the equation was solved using the fourth order Runge-Kutta method. Chen [10] reported an innovative mechanism design method for achieving the feasible mechanisms that satisfied the requirements of the CB. The kinematic and dynamic equations of the mechanism were derived through the vector loop method, and the Lagrange equation was solved using the Runge-Kutta method. Based on the total energy conservation in a spring-actuated linkage system throughout its operating range, Ahn et al. [2] developed a systematic procedure to optimize the spring design parameters for achieving the desired opening and closing characteristics of the electric contacts in a VCB. The spring parameters were optimized to minimize the sum of the squares of the errors between the desired and calculated rotating velocities using the modified simplex method. Yoo et al. [11] analyzed the dynamic characteristics of the spring-actuated operating mechanism of the CB using ADAMS. Yu et al. [12] optimized the dimensional synthesis of the trigger mechanism of a 24-kV CB to minimize both the response time of the trigger hook and contact stress between the cam and roller follower. To achieve a shorter circuit breaking time, Jang et al. [13] developed a multibody dynamic model of a CB, including a switch mechanism that was optimized using a genetic algorithm (GA), and a multibody dynamic analysis of the optimum mechanism was performed using MSC-ADAMS. The opening time of the mechanism was decreased by 2.3 ms, as validated through experiments. Liu et al. [14] proposed an optimum design method for the cam design structure of a molded case circuit breaker (MCCB) and used ADAMS to perform dynamic simulations. The results indicated that the optimal cam design structure effectively prevented the movable conductor from returning when the short-circuit current was  $\geq 15$  kA and enhanced the interruption performance of the MCCB. Storn and Price [15] proposed a differential evolution (DE) algorithm to minimize possible nonlinear and non-differential continuous space functions. Several studies have focused on the applications of the DE algorithm and its variants for the optimal design of path-generating four-bar linkages. For example, Acharyya et al. [16], compared the optimal results obtained using the DE algorithm with those obtained using a genetic algorithm (GA) and particle swarm optimization (PSO) algorithm; they inferred that the DE method was superior to the GA and PSO methods [16]. Lin [17] used a GA-DE hybrid algorithm combined DE with a real-valued genetic algorithm. Ortiz et al. [18] used an improved DE algorithm with self-adaptive control parameters (called IOA<sup>s-at</sup> method). Recently, Kang et al. [19] applied the DE algorithm with a specified golden ratio (0.618:0.382) as the cross rate and mutation factor; the method is called the DE-gr method, to effectively optimize the dimensional synthesis problem of path-generating four-bar linkages. They reported that the efficiency and accuracy of the DE-gr algorithm was superior to those of the PSO, DE [16], DE-GE [17] and IOA<sup>s-at</sup> [18] methods.

The objective of present study is to optimally design a VCB mechanism, a spring-actuated cam-linkage operating mechanism with rated voltage 12 kV and rated short circuit current 25 kA, and to perform the dynamic analysis of the optimal VCB mechanism. The novel approach of this work is to present an objective function of optimization that minimizes the surplus output work in the VCB operating mechanism during the closing operation, such that the average closing velocity of the moving contact and the Hertz contact stress on the cam surface are decreased to satisfy the design requirements. Consequently, the

net difference between the general output force and the general resistant force of the VCB operating mechanism during the closing process was considered as the objective function to be minimized, and a DE algorithm with golden ratio (DE-gr) was employed to successfully optimize the design of the VCB operating mechanism, which are the contributions of this work.

The remainder of this paper is organized as follows: Section 2 describes the actuation principle and design of the spring-actuated cam-linkage composite operating mechanism of a VCB. Then, the characteristic forces (spring forces and active forces between different parts) and Hertz contact stress between the cam and roller follower of initial VCB mechanism design are discussed. Section 3 describes the multibody dynamic simulation of the VCB operation mechanism using MSC-ADAMS. Section 4 introduces the differential evolution (DE) algorithm and the optimization procedure. The optimal design of the cam and closing springs using the DE-gr method and the dynamic analysis of the optimal VCB mechanism were performed firstly, followed by the optimal design and dynamic analysis of the four-bar linkage and the optimal VCB mechanism, respectively. Finally, Section 5 draws the conclusions of the study.

## 2. Design of the VCB Operating Mechanism

### 2.1. Actuation Principle and Specified Motion of the VCB Operating Mechanism

A medium-voltage VCB is composed of two components: the vacuum interrupter (VI) and the operating mechanism. The operating mechanism was designed for opening and closing the electric contacts in the VI. In the VI, the electric movable contact and fixed contact were installed in a ceramic insulator envelope wherein high vacuum approximately  $10^{-5}$  Pa was maintained. The employed operating mechanism in the present study was a spring-actuated cam-linkage composite mechanism, and the main constituent parts are illustrated in Figures 1 and 2, comprising a cam and follower mechanism, a four-bar linkage, a hook, an insulated rod, and three different springs (closing spring, opening spring, and contact spring). The movable contact for each of three phases was connected to the operating mechanism through an insulated rod and contact spring (also called a wipe spring). Figures 1 and 2 illustrate the basic configurations of the VCB operating mechanism in its opened state and closed state, respectively. In the closed state, the electric system was normally operational because the movable contact engaged with the fixed contact, and the current was connected between the primary and secondary ends; however, in the opened state, the electric current was interrupted because the movable contact separated from the fixed contact.

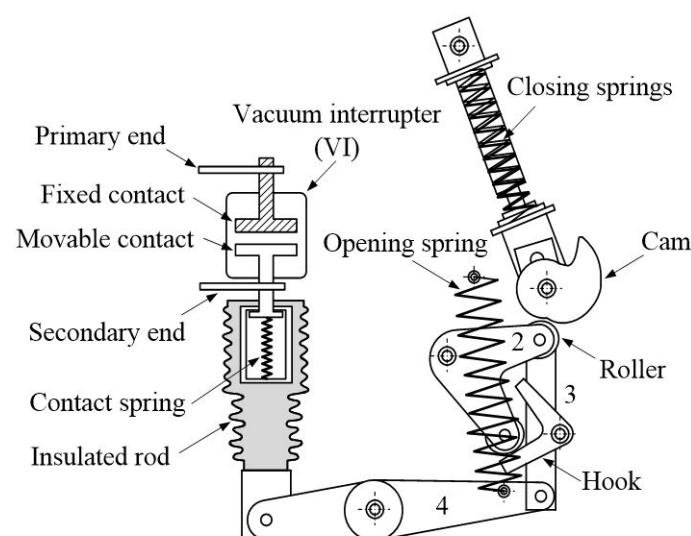


**Figure 1.** Opened state of a spring-actuated mechanism.

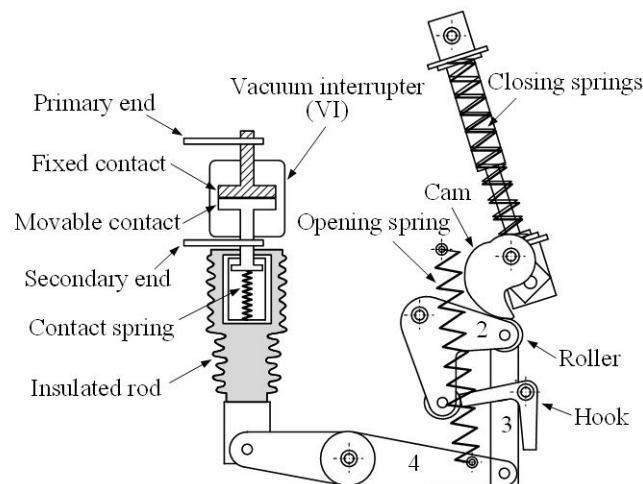


**Figure 2.** Closed state of a spring-actuated mechanism.

In the opened state (Figure 1), two closing springs (with different stiffness) eccentrically connected to the axis of the cam were initially compressed using a motor (not shown), and elastic energy was stored. Once a closing command was received, the closing springs were automatically or manually actuated, and the stored energy was used to drive the cam and roller follower and to drive the four-bar linkage wherein the output link would synchronously drive the insulated rod and movable contact upward. Meanwhile, the elastic energy was stored in the opening spring. When the movable contact engaged with the fixed contact, the insulated rod continued to move upward and compressed the contact spring in the VI. When the stored energy of the closing springs was exhausted, the hook automatically latched onto the roller to prevent the VCB from rebounding and completed the switching action from the opened state to the closed state.

By contrast, when an opening command was received, the contact spring and opening spring concurrently released the stored energy and the hook unlatched, thereby driving the insulated rod and movable contact rapidly downward and restoring the VCB to the opened state. The performance of the VCB was primarily affected by the materials of the electric contacts and the average closing velocity of the movable contact. The average closing velocity was defined as the average velocity of the movable contact within the last 1/3 contact stroke, and the average opening velocity was defined as the average velocity within the 3/4 range of the contact stroke from the moment of the moving contact departure [20]. If the average closing velocity of the movable contact was exceedingly high, it would cause high contact bounding, electric arc occurrence, and damage to the VCB. This studied attempted to reduce the high average closing velocity of the moving contacts for improving the performance of the VCB and to thus minimize the surplus work of the VCB operating mechanism during the closing process.

Figure 3 illustrates the status of the cam-linkage composite operating mechanism of the VCB when switching from the opened state (indicated by a dashed line) to the closed state. During cam rotation with high angular velocity, the roller followers continuously make contact with the cam, thereby preventing adverse dynamic responses. As illustrated in Figure 3,  $\theta_c$  denotes the rotation angle of the cam,  $s_1$  and  $s_2$  (both in the positive direction with the increase in  $\theta_c$ ) represent the vertical displacement of points L and M on the output link of the four-bar linkage, respectively. At  $\theta_c = 140^\circ$ , the point L moved to the lowest position of the motion, where the overall vertical displacement was  $\bar{s}_2$ . Concurrently, point M moved an overall vertical distance of  $\bar{s}_1$ , while the movable contact moved a contact stroke  $s_c$ . Subsequently, the hook latched onto the follower link BD and prevented the opening spring from retracting the link. Within a complete revolution of the cam, the rotation angle required for the cam to effectively contact the roller and complete the closing operation was less than  $180^\circ$ , and the contact between the cam and the roller should be prevented in the remainder cam rotation angle. The vertical displacement ( $s_2$ ) of point L

exhibited a nonlinear relationship with the rotation angle of the cam ( $\theta_c$ ) during the closing operation. The nonlinear motion relationship between  $s_2$  and  $\theta_c$  is illustrated in Figure 4 and depends on the characteristics of the CB, displacement range of the insulated rod, and the required average velocity of the movable contact ( $1.5 \pm 0.2$  m/s for the opening operation;  $0.9 \pm 0.2$  m/s for the closing operation). The motion relation was specified using the cam rotation angle  $\theta_{ci}$  ( $i = 0, 1, 2, 3$ ) at  $0^\circ, 70^\circ, 100^\circ,$  and  $140^\circ$ , the corresponding vertical displacements of point L were  $s_{20} = 0, s_{21} = 0.7\bar{s}_2, s_{22} = 0.9\bar{s}_2,$  and  $s_{23} = \bar{s}_2$ , respectively, and the corresponding rotation angles of the output link LE of the four-bar linkage were  $\theta_{40} = 0, \theta_{41} = 0.7\bar{\theta}_4, \theta_{42} = 0.9\bar{\theta}_4,$  and  $\theta_{43} = \bar{\theta}_4$ , respectively;  $\bar{\theta}_4$  is the overall angular displacement of the output link 4. The motion relationship was similar to that between the motion of the roller follower and the cam.

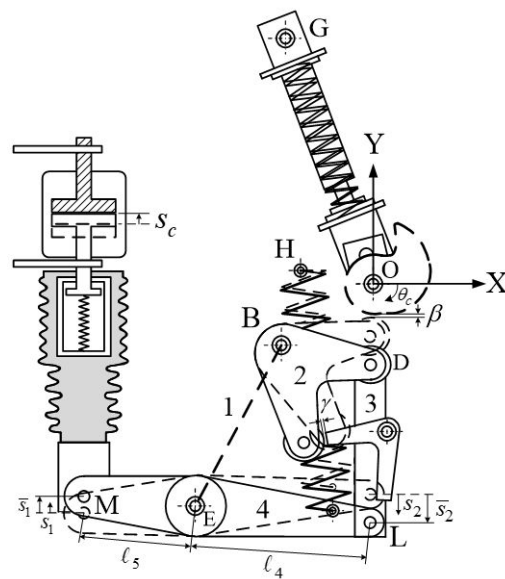


Figure 3. Sketch for closing motion of a spring-actuated operating mechanism.

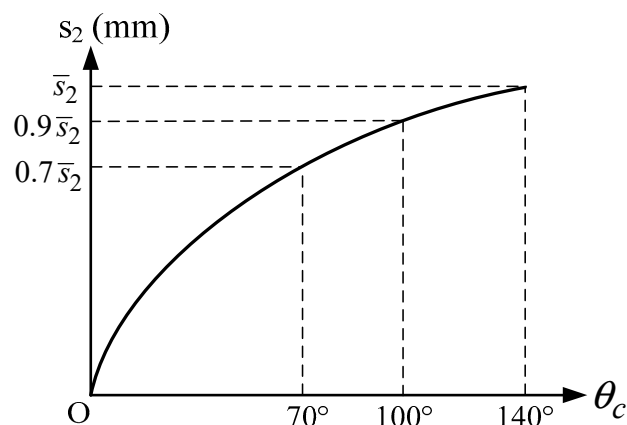


Figure 4. Specified motion relation of the VCB operating mechanism during closing process.

## 2.2. Cam Profile Design of the VCB Operation Mechanism

In the cam profile design, the design of the motion curve of the follower dominantly affected the output force characteristics of the VCB mechanism and the closing velocity of the movable contact, thereby influencing the overall performance of the VCB. The cam profile was designed based on the theorem of mechanisms [21], and the four-bar linkage was analyzed. Rectangular coordinate systems were used to design the cam profile (Figure 5). In Figure 5, x-y and X-Y represent the coordinate systems for the cam and the

VCB system, respectively. Point O indicates the origin of the coordinate system;  $x'-y'$  is the coordinate system that represents the actual assembly of the cam on the VCB.

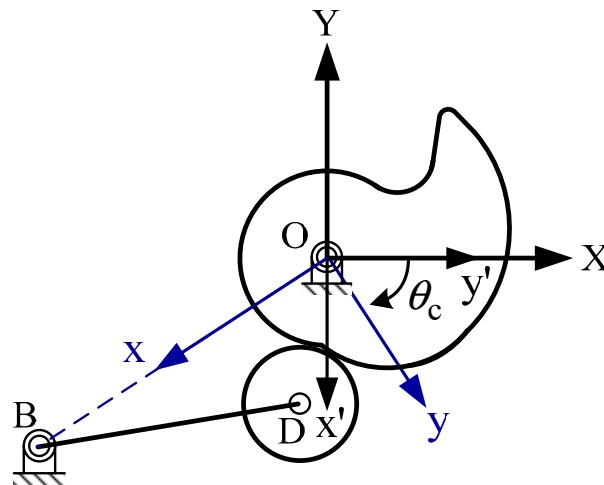


Figure 5. Coordinate systems of the cam mechanism.

The procedures of the cam profile design are described as follows:

Step 1. Assuming the oscillating angle of output link LM was very small, and the triangular proportions of the two limit positions of link LM at the opened and closed states were similar (Figure 3). Based on these, in addition to practical clearance design considerations, the instantaneous vertical displacements of points L and M,  $s_2$ , and  $s_1$  are approximated as follows:

$$s_2 = \frac{1}{\alpha} \left( \frac{\ell_4}{\ell_5} \right) s_1 + \beta + \gamma \tag{1}$$

where,  $\ell_4$ ,  $\ell_5$  denote the lengths of the two sides of output link,  $\alpha$  denotes the loss coefficient of contact,  $\beta$  denotes the required initial clearance between the cam and roller, and  $\gamma$  denotes the required initial clearance between the hook and roller. The values of  $\alpha$ ,  $\beta$  and  $\gamma$  are based on empirical knowledge.

Step 2. A known  $\bar{s}_1$  condition is incorporated into Equation (1) to determine  $\bar{s}_2$ .

Step 3. Because the length of link 2 ( $\ell_2$ ) and the clearance ( $\beta$ ) between the roller and cam are known, the initial angular position of input link 2 ( $\theta_{20}$ ) (Figure 6) of the four-bar linkage are determined as follows:

$$\theta_{20} = \tan^{-1} \left( \frac{B_y}{B_x} \right) - \cos^{-1} \left[ \frac{\ell_2^2 + \ell_6^2 - (r_b + r_f + \beta)^2}{2\ell_2\ell_6} \right] \tag{2}$$

where,  $r_b$  is the radius of base circle of cam and  $r_f$  is the radius of roller follower.  $(B_x, B_y)$  is the coordinate of the pivot point B, and  $\ell_6$  is the distance between two pivot points B and O.

Step 4. If the preset angle of fixed link ( $\theta_1$ ) and initial input angle ( $\theta_{20}$ ) of link 2 are given, the initial output angle ( $\theta_{40}$ ) of link 4 are expressed as follows (Figure 6) [21]:

$$\theta_{40} = 2 \tan^{-1} \left( \frac{B_0 + \sqrt{A_0^2 + B_0^2 - C_0^2}}{A_0 + C_0} \right) \tag{3}$$

where

$$\begin{aligned} A_0 &= 2\ell_1\ell_4 \cos \theta_1 - 2\ell_2\ell_4 \cos \theta_{20} \\ B_0 &= 2\ell_1\ell_4 \sin \theta_1 - 2\ell_2\ell_4 \sin \theta_{20} \\ C_0 &= \ell_3^2 - \ell_1^2 - \ell_4^2 - \ell_2^2 + 2\ell_1\ell_2 \cos(\theta_{20} - \theta_1) \end{aligned}$$

$\ell_1, \ell_2, \ell_3$  and  $\ell_4$  are the lengths of the four-bar linkage.

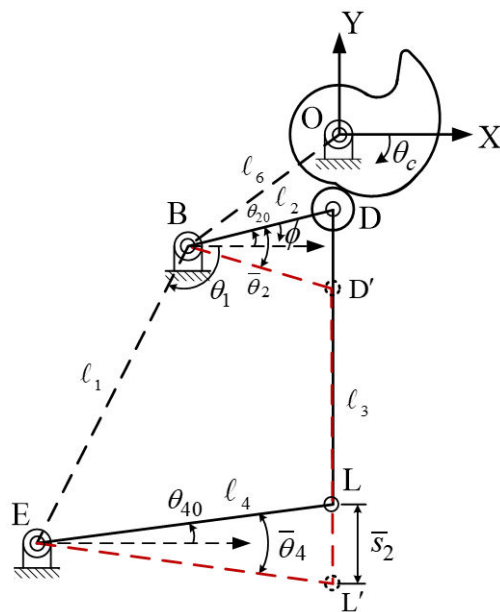


Figure 6. Cam and four-bar linkage composite mechanism.

Step 5. When the known conditions and Equation (1) are used, the overall angular displacement ( $\bar{\theta}_4$ ) of the output link can be determined through trigonometry (Figure 6).

$$\bar{\theta}_4 = 2 \sin^{-1}\left(\frac{\bar{s}_2}{2l_4}\right) \tag{4}$$

Subsequently,  $\theta_{4i}$  ( $i = 1, 2, 3$ ) can be obtained using Equations (1) and (4) and the associations of  $\theta_{ci}$  ( $i = 1, 2, 3$ ) shown in Figure 4.

Step 6. When  $\bar{\theta}_4$  and  $\theta_{4i}$  ( $i = 1, 2, 3$ ) of the four-bar linkage were determined, the corresponding angular position of link 2,  $\theta_{2i}$  ( $i = 1, 2, 3$ ), are determined as follows:

$$\theta_{2i} = 2 \tan^{-1}\left(\frac{B_i - \sqrt{A_i^2 + B_i^2 - C_i^2}}{A_i + C_i}\right) \quad (i = 1, 2, 3) \tag{5}$$

where

$$\begin{aligned} A_i &= -2l_1l_2 \cos \theta_1 - 2l_2l_4 \cos \theta_{4i} \\ B_i &= -2l_1l_2 \sin \theta_1 - 2l_2l_4 \sin \theta_{4i} \\ C_i &= l_3^2 - l_1^2 - l_4^2 - l_2^2 - 2l_1l_4 \cos(\theta_{4i} - \theta_1) \end{aligned} \quad (i = 1, 2, 3)$$

Step 7. Because the oscillating follower link BD of the cam mechanism serves as the input link of the four-bar linkage, according to the specified motion of the VCB mechanism displayed in Figure 4, four angular positions of the follower link ( $\phi_i$ ,  $i = 0, 1, 2, 3$ ) must satisfy the restriction. Therefore, a three-order polynomial displacement curve of the follower was employed to design the cam profile for preventing the occurrence of discontinuous acceleration of the follower, which may lead to transmission shock, noise, concentrated stress, and wear on the cam surface and eventually damage the cam. The three-order polynomial displacement function contains four unknown coefficients ( $a_0, a_1, a_2$  and  $a_3$ ) is expressed as follows:

$$\phi(\theta_c) = a_0 + a_1\theta_c + a_2\theta_c^2 + a_3\theta_c^3 \tag{6}$$

The relationship between the angular positions of the follower link BD ( $\phi_i$ ,  $i = 0, 1, 2, 3$ ) and rotation angles of the cam ( $\theta_{ci}$ ,  $i = 0, 1, 2, 3$ ) is expressed as follows:

$$\begin{cases} \theta_{c0} = 0, & \phi_0 = ? \\ \theta_{c1} = 70^\circ, & \phi_1 = |\theta_{21} - \theta_{20}| \\ \theta_{c2} = 100^\circ, & \phi_2 = |\theta_{22} - \theta_{20}| \\ \theta_{c3} = 140^\circ, & \phi_3 = |\theta_{23} - \theta_{20}| \end{cases} \quad (7)$$

Step 8. In the initial default position of the cam, a clearance  $\beta$  is retained between the cam and roller follower to prevent the roller from colliding with the cam at the instant of the operating mechanism to restore its default position. Therefore, at the initial default position the distance between the centers of cam and roller is  $r_p = r_b + r_f + \beta$ . Subsequently, the cam must be rotated counter clockwise with a small angle  $\theta_0$ , covering a distance of  $\beta$  relative to the roller. Therefore, the actual rotation angle of the cam,  $\theta$ , in the operating mechanism is  $\theta = \theta_0 + \theta_c$ . When  $\theta_{c0} = 0$ , according to the geometric association illustrated in Figure 7, the initial angular position of the follower link BD ( $\phi_0$ ) is determined as follows:

$$\phi_0 = \cos^{-1} \left[ \frac{\ell_2^2 + \ell_6^2 - r_p^2}{2\ell_2\ell_6} \right] - \cos^{-1} \left[ \frac{\ell_2^2 + \ell_6^2 - (r_b + r_f)^2}{2\ell_2\ell_6} \right] \quad (8)$$

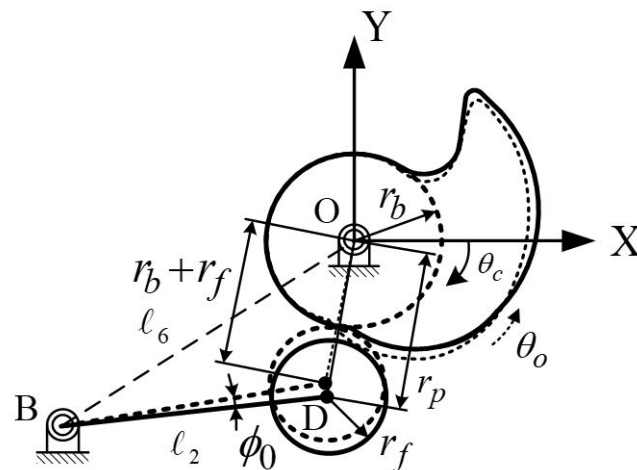


Figure 7. Initial setting of the cam mechanism with a clearance.

Step 9. From Equations (5) to (7), four simultaneous equations are used to determine the four unknown coefficients:  $a_0, a_1, a_2,$  and  $a_3$ .

Step 10. According to Figure 8, the coordinates  $(x_p, y_p)$  of the pitch curve of the cam is determined using the following equations [21]

$$\begin{aligned} x_p &= \ell_6 \cos \theta_c - \ell_2 \cos(\theta_c - \xi - \phi) \\ y_p &= \ell_6 \sin \theta_c - \ell_2 \sin(\theta_c - \xi - \phi) \end{aligned} \quad (9)$$

where

$$\xi = \cos^{-1} \left[ \frac{\ell_2^2 + \ell_6^2 - (r_b + r_f)^2}{2\ell_2\ell_6} \right] \quad (10)$$

Step 11. The coordinates of the cam profile  $(x_c, y_c)$  are determined using the following equations

$$\begin{aligned} x_c &= x_p - r_f \left( \frac{dy_p}{d\theta_c} \right) \left[ \left( \frac{dx_p}{d\theta_c} \right)^2 + \left( \frac{dy_p}{d\theta_c} \right)^2 \right]^{-1/2} \\ y_c &= y_p + r_f \left( \frac{dx_p}{d\theta_c} \right) \left[ \left( \frac{dx_p}{d\theta_c} \right)^2 + \left( \frac{dy_p}{d\theta_c} \right)^2 \right]^{-1/2} \end{aligned} \quad (11)$$



where

$$\begin{aligned} \frac{dx_p}{d\theta_c} &= -l_6 \sin \theta_c + l_2 \left(1 - \frac{d\phi}{d\theta_c}\right) \sin(\theta_c - \xi - \phi) \\ \frac{dy_p}{d\theta_c} &= l_6 \cos \theta_c - l_2 \left(1 - \frac{d\phi}{d\theta_c}\right) \cos(\theta_c - \xi - \phi) \\ \frac{d\phi}{d\theta_c} &= \phi' = a_1 + 2a_2\theta_c + 3a_3\theta_c^2 \end{aligned} \tag{12}$$

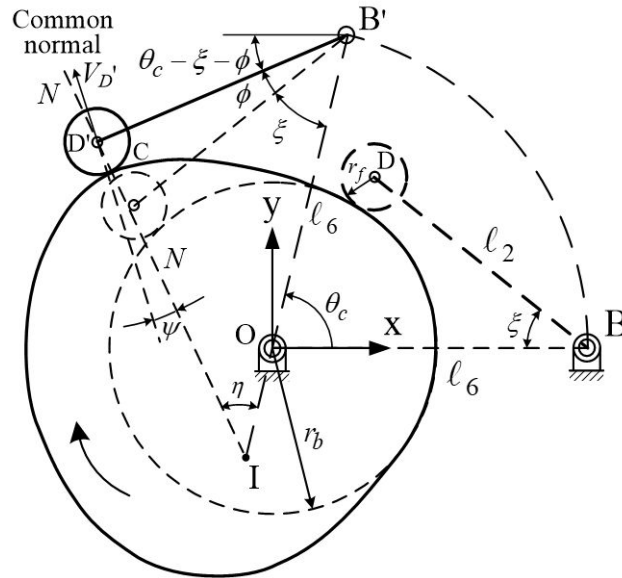


Figure 8. Disc cam with an oscillating roller follower.

Step 12. The pressure angle ( $\psi$ ) of the cam, which is defined as the angle between the linear velocity ( $V_D$ ) of the center of the roller follower and the common normal on the contact surfaces (Figure 8), is expressed as follows

$$\psi = \frac{\pi}{2} - \eta - \xi - \phi \tag{13}$$

As displayed in Figure 8, the intersection point, I, between the common normal of the contact surfaces and the lines joining the two rotation axes, is the instantaneous center of the follower motion relative to the cam, and can be determined using trigonometry.

$$\eta = \sin^{-1} \left[ \frac{l_2 \sin(\xi + \phi)}{\overline{ID'}} \right] \tag{14}$$

where

$$\begin{aligned} \overline{ID'} &= \sqrt{l_2^2 + (\overline{OI} + l_6)^2 - 2l_2(\overline{OI} + l_6) \cos(\xi + \phi)} \\ \overline{OI} &= \left(\frac{l_6}{1-\phi'}\right)\phi' \end{aligned}$$

Step 13. The radius of curvature ( $\rho_c$ ) of the cam profile is subsequently determined [21].

$$\rho_c = \frac{\left[ l_6^2 - 2l_2l_6 \cos(\xi + \phi)(1 - \phi') + l_2^2(1 - \phi')^2 \right]^{3/2}}{l_6^2 - l_2l_6(2 - \phi')(1 - \phi') \cos(\xi + \phi) - l_2l_6(\phi'') \sin(\xi + \phi) + l_2^2(1 - \phi')^3} - r_f \tag{15}$$

where

$$\phi'' = \frac{d\phi'}{d\theta_c} = 2a_2 + 6a_3\theta_c$$

The radius of curvature of the cam profile is crucial for calculating the Hertz contact stress between the contact surfaces of the cam and roller follower. The Hertz contact stress

was evaluated to determine whether the contact stress and the shear stress of the cam surface were lower than the endurance contact stress and yielding shear stress, respectively.

A clearance  $\beta$  must be retained between the cam and the roller to prevent the roller from colliding with the cam during the operating mechanism to restore its default position.

### 2.3. Kinematic Analysis of the Initial VCB Mechanism Design

Figure 9 displays the schematic of a spring-actuated cam-linkage composite operating mechanism of a VCB during the closing operation. The data and design parameters of the initial design provided by the manufacturing vendor were as follows (Figures 3 and 9). Data of four-bar linkage:  $l_1 = 139.79$  mm,  $l_2 = 70$  mm,  $l_3 = 124.7$  mm,  $l_4 = 140$  mm,  $l_5 = 90$  mm,  $l_6 = 90.6035$  mm,  $l_7 = 105$  mm, and  $l_8 = 25$  mm; the overall vertical displacement of point M,  $\bar{s}_1 = 16$  mm, the coordinates of fixed pivots were G(50, 200), O(0, 0), H(-57, 19), B(-72, -55), and E(-142, -176), and the angle  $\angle LES$  was  $4.9^\circ$ ; the preset angle  $\angle QOX$  was  $95^\circ$ . Data of the cam mechanism: radius of base circle of the cam was  $r_b = 23$  mm, radius of the roller follower was  $r_f = 15$  mm, loss coefficient of the contact was  $\alpha = 0.95$ , clearance between the roller and hook was  $\gamma = 1$  mm, clearance between the cam and roller was  $\beta = 2$  mm, and the default initial rotation angle was  $\theta_0 = 4^\circ$ . The kinematic analysis of the initial design of the VCB operating mechanism was performed during the closing operation using a MATLAB coded program.

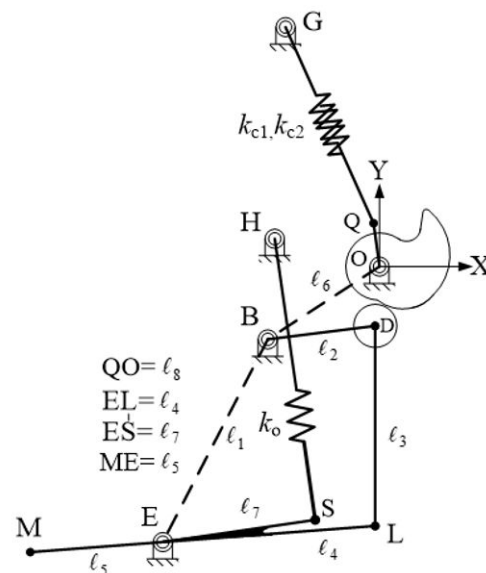


Figure 9. Sketch of the VCB operating mechanism during closing process.

According to Equations (5) to (8), the four coefficients of the three-order polynomial displacement curve of the follower were determined as follows:  $a_0 = 0.015185$ ,  $a_1 = 0.240347$ ,  $a_2 = 0.011694$ ,  $a_3 = -0.017243$ . Figures 10–13 illustrate the results of kinematic analysis of the initial cam design. Figure 10 only displays the portions of the pitch curves and the cam profile that make continuous contact with the roller. Figure 11 (red dashed line) illustrates the angular displacement curve of the oscillating follower. Figure 12 (red dashed line) displays the pressure angle of the cam mechanism; the maximum pressure angle was less than the allowable maximum pressure angle of  $45^\circ$ . Figure 13 (red dashed line) depicts the radii of curvature of the cam profiles that are greater than the radius of the roller (15 mm), that is,  $\rho_c > r_f$ , indicating that no undercutting occurred on the cam profile. Thus, if considering only the curvature of cam profile, the initial cam design was feasible. For reducing the number of figures and facilitating the comparison between the initial cam design and optimal cam design discussed in Section 4, the relevant analyses curves (blue solid line in Figures 11–13) of the optimized cam mechanism were included into the figures of the analyses of initial design.

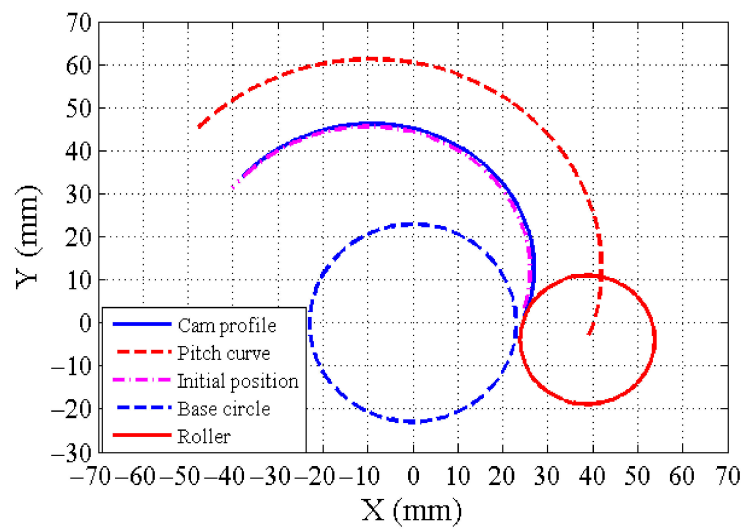


Figure 10. Initial cam profile and pitch curve (only actuated portion).

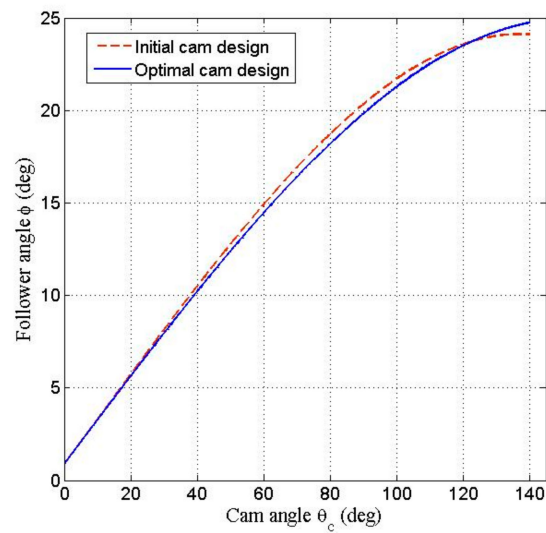


Figure 11. Angular displacement curve of the oscillating follower.

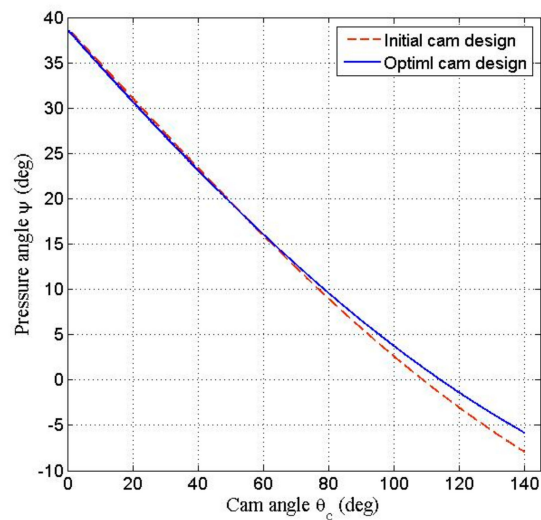


Figure 12. Pressure angle of the cam mechanism.

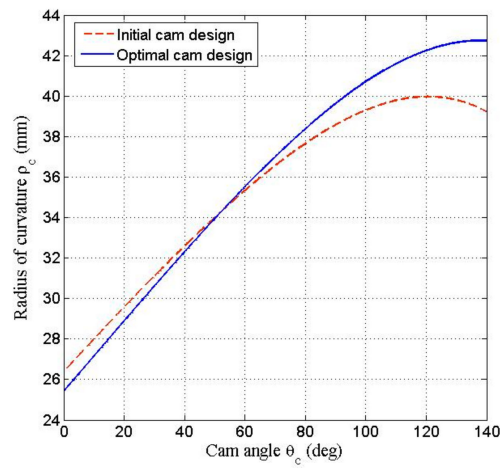


Figure 13. Radius of curvature of the cam profile.

Figure 14 (red dashed line) displays the displacement function curve of point L. Both red dashed lines in Figures 10 and 14 depict similar motion relationships. The relationship between the output and input angles of the four-bar linkage was approximately linear, as illustrated by red dashed line in Figure 15.

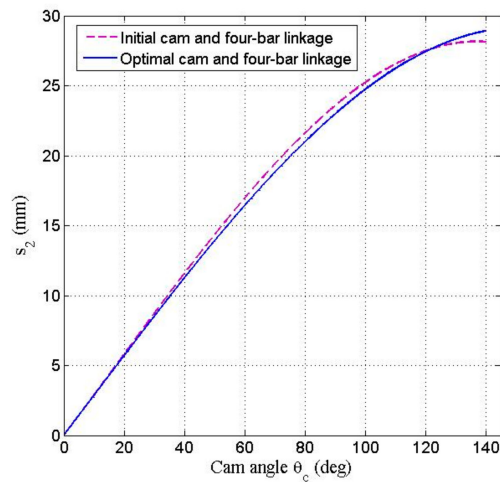


Figure 14. Displacement function curve of point L.

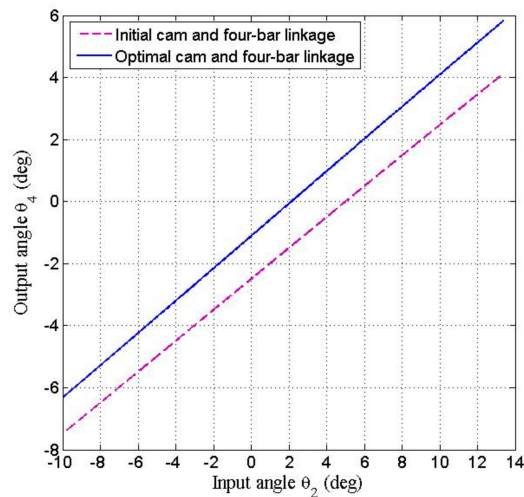


Figure 15. Output-input curve of the four-bar linkage.



During the closing operation, the active forces between the various parts of the mechanism were assumed to be quasi-static and were determined by applying the concept of moment equilibrium to the FBD of the various parts.

The FBD of the cam (Figure 16a) is represented by the following relationship:

$$F_n = \frac{r_1}{r_2} F_{cs} \quad (19)$$

where  $F_n$  denotes the instantaneous normal contact force between the cam and the roller follower, and  $r_1$ ,  $r_2$  represent the instantaneous perpendicular distance (or force arm) from the line of corresponding active force.

The FBD of the roller and follower link (Figure 16b) is represented by the following relationship:

$$F_3 = \frac{r_3}{r_4} F_n = \frac{r_1 r_3}{r_2 r_4} F_{cs} \quad (20)$$

where  $F_3$  is the transmission force on the connecting link 3, and  $r_3$ ,  $r_4$  represent the instantaneous perpendicular distance from the line of corresponding active force.

As depicted in the FBD of the output link LM connected to the insulated rod and movable contact (Figure 16c), the moment exerted on the main shaft E of the output link, referred to as the driving moment ( $M_d$ ), originated in two closing springs, and the resistant moment ( $M_r$ ), originated in the opening spring, three contact springs, and atmospheric pressure force. The driving moment and resistance moment are expressed as follows:

$$M_d = r_5 F_3 \quad (21)$$

$$M_r = r_7 F_{os} + r_6 (F_w - F_{fc}) \quad (22)$$

where  $r_5$ ,  $r_6$  and  $r_7$  denote the instantaneous perpendicular distance from the line of corresponding active force.

To effectively achieve a closed state, the driving moment  $M_d$  exerted on the output link should have been greater than the resistant moment  $M_r$ ,  $M_d > M_r$ . Regarding the work done in the subsystem, as displayed in Figure 16c, the net work done on the main shaft E by the driving moment and resistant moment (assuming neglecting the effect of friction forces on joints) should be positive during the closing operation. The net done work ( $U_{net}$ ) is expressed as follows:

$$\begin{aligned} U_{net} &= \int_0^{\bar{\theta}_4} (M_d - M_r) d\theta_4 \\ &= \int_0^{\bar{\theta}_4} \left[ r_5 F_3 - \left( r_7 F_{os} + (F_w - F_{fc}) r_6 \right) \right] d\theta_4 \\ &= \int_0^{\bar{s}_2} F_3 ds_2 - \int_0^{\bar{s}_1} \left[ \left( \frac{r_7}{r_6} \right) F_{os} + F_w - F_{fc} \right] ds_1 \\ &= \int_0^{\bar{s}_1} \left\{ \left( \frac{\ell_4}{\alpha \ell_5} \right) F_3 - \left[ \left( \frac{r_7}{r_6} \right) F_{os} + F_w - F_{fc} \right] \right\} ds_1 \\ &= \int_0^{\bar{s}_1} \left\{ \left( \frac{r_1 r_3 r_5}{r_2 r_4 r_6} \right) F_{cs} - \left[ \left( \frac{r_7}{r_6} \right) F_{os} + F_w - F_{fc} \right] \right\} ds_1 > 0 \end{aligned} \quad (23)$$

In Equation (23),  $r_5 d\theta_4 = ds_2$ ,  $r_6 d\theta_4 = ds_1$  and from Equation (10),  $ds_2 = \ell_4 / (\alpha \ell_5) ds_1 = (r_5 / r_6) ds_1$ . The first term and second term in the bracket of above equation can be referred as the general output force ( $F_o$ ) and general resistant force ( $F_r$ ) of the VCB operating mechanism, respectively.

$$F_o = \left( \frac{r_1 r_3 r_5}{r_2 r_4 r_6} \right) F_{cs}, \quad F_r = \left( \frac{r_7}{r_6} \right) F_{os} + F_w - F_{fc} \quad (24)$$

The general output force was affected by the closing spring force ( $F_{cs}$ ) and the force arms ( $r_1, r_2, \dots, r_6$ ) were strongly affected by the cam profile and the dimensions of the four-bar linkage. The general resistant force was affected by the opening spring force ( $F_{os}$ ),

contact spring force ( $F_w$ ), free contact force ( $F_{fc}$ ) and the force arms ( $r_6, r_7$ ). Because the small rotation angle of the link LM, the change in  $r_6$  and  $r_7$  were considerably small and the stiffness of opening spring and contact spring were not in the design parameters, the general resistant force during the closing operation was approximately the same in the various VCB operating mechanisms designed in this study.

Equation (23) can be expressed as

$$U_{net} = \int_0^{\bar{s}_1} (F_o - F_r) ds_1 > 0 \cong \sum_{i=1}^{N_s} (F_o - F_r)_i \delta s_i > 0 \quad (25)$$

where  $N_s$  is the position number selected to calculate the forces, and  $\delta s$  is the small step displacement of the insulated rod. In Equation (25), the larger the value of  $N_s$ , the closer it is to the definite integral of Equation (23). Considering the energy loss due to the friction forces acting on the joints of the VCB mechanism, the VCB mechanism system was assumed to have a mechanical efficiency of 85% ( $\varepsilon = 0.85$ ), therefore, Equation (25) was modified as follows

$$U_{net} \cong \sum_{i=1}^{N_s} (F_{oi} - \frac{F_{ri}}{\varepsilon}) \delta s_i > 0 \quad (26)$$

Based on above derived equations, a MATLAB2011 coded program was developed for analyzing the characteristic forces (including spring forces, general output force, and general resistant force), and the displacement of the insulated rod during closing operation in the VCB mechanism. The program was executed using an ASUS-P43E notebook with Intel core I5-2450M 2.5 GHz CPU. The various characteristic forces, including the opening spring force (red dashed line), closing spring force (black dashed line), wipe spring force (solid green line), general resistant force (red line) and general output force (blue dashed line) during the closing operation were displayed in Figure 17. The general output force of the VCB operating mechanism is not always required to be greater than the general resistant force during the closing stroke. The area under curve (AUC) of the general output force represents the integration of the force with respect to the differential displacement of the insulated rod, indicating the output work (also referred to as driving work) in the VCB operating mechanism. Similarly, the AUC of the general resistant force indicates the resistant work in the VCB operating mechanism. This study aimed to minimize the net work done (or referred as surplus output work, equal to the difference of the driving work and the resistant work) for the CVB operating mechanism during the closing operation. Therefore, if the value of  $N_s$  was taken large enough, considering that the step increment of insulated rod was differential and constant, the overall differences between the general output forces and the general resistant forces (divided by mechanical efficiency) at the selected sequence positions of the insulated rod during the closing operation was considered as the objective function to be minimized, as discussed in Section 4.

Two elastic contact bodies with various curvatures cannot form a line or point contact. The contact formed in such a case is extremely small with high stress values, commonly known as Hertz contact stress [22,23]. The contact pattern between the cam and the cylindrical roller exhibited a rectangular shape as depicted in Figure 18. The contact stress distribution resembled a semi-elliptical prism of half-width  $b$ . The contact rectangular measuring  $2b$  (width)  $\times \ell$  (length), and the half-width ( $b$ ) of the rectangular is expressed as follows:

$$b = \sqrt{\frac{8F_n \rho_e}{\pi \ell E_e}} \quad (27)$$

where  $\rho_e$  denotes the equivalent radius of curvature at the contact surfaces,  $F_n$  denotes the normal contact force and  $E_e$  denotes the equivalent elastic modulus, as represented by following equations:

$$\frac{1}{\rho_e} = \frac{1}{\rho_c} + \frac{1}{\rho_r} \quad (28)$$

$$\frac{1}{E_e} = \frac{1}{2} \left( \frac{1 - \nu_1^2}{E_1} + \frac{1 - \nu_2^2}{E_2} \right) \tag{29}$$

where  $E_1$  and  $E_2$  denote the elastic modulus of the cam and roller, respectively;  $\nu_1$  and  $\nu_2$  denote Poisson’s ratios of the cam and roller, respectively. The maximum Hertz contact stress ( $\sigma_{max}$ ) is generated at the center of the contact surface between the cam and the roller follower and can be expressed as follows:

$$\sigma_{max} = \frac{2F_n}{\pi b \ell} \tag{30}$$

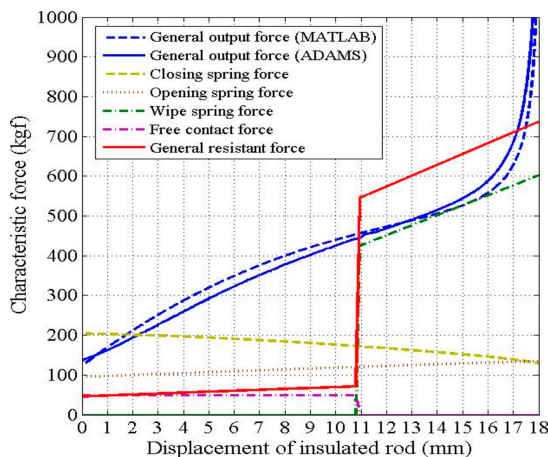


Figure 17. Characteristic forces during closing process for the initial VCB mechanism deign.

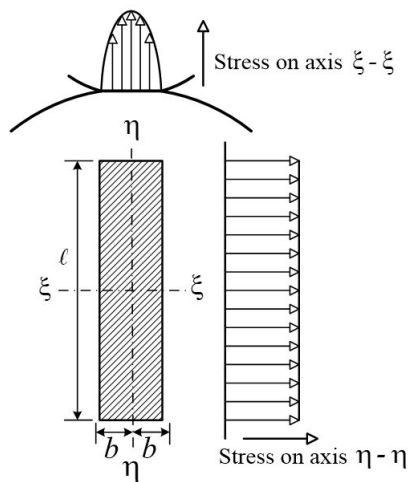


Figure 18. Contact pattern between the cam and cylindrical roller.

If the cam and roller follower are manufactured using the same steel material (Poisson’s ratio  $\nu = 0.3$ ), the maximum shear stress ( $\tau_{max}$ ) occurs at approximately  $0.786b$  beneath the surface of the cam and can be expressed as follows:

$$\tau_{max} = 0.304\sigma_{max} \tag{31}$$

The maximum shear stress is a crucial factor that determines the surface failure of the cam that begins with an initial crack beneath the surface [23,24]. The maximum Hertz contact stress on the cam surface of the initial VCB mechanism is depicted in Figure 19, and a considerably high Hertz stress occurred near the end of closing stroke. The maximum shear stress beneath the cam surface is depicted in Figure 20. According to the Mises-Hencky shear yielding criteria [25] and Table 1, the shear yielding stress ( $\tau_y$ ) of the carbon



steel (S45C) is  $\tau_y = 0.577\sigma_y = 1194$  MPa. Figure 20 illustrates that the maximum value of maximum shear stress was larger than the shear yielding stress, and thus the initial VCB mechanism design was not feasible.

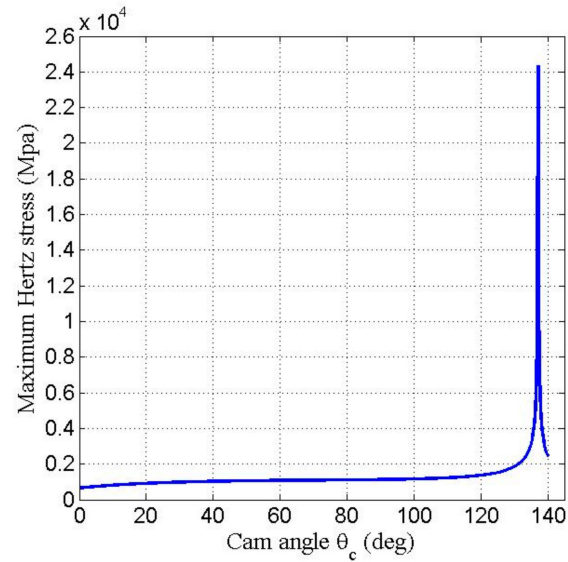


**Figure 19.** Maximum Hertz contact stress on the cam surface of the initial design.

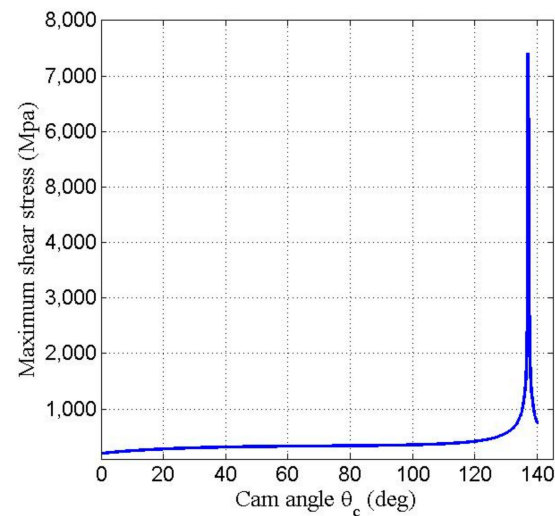


**Figure 20.** Maximum shear stress beneath the cam surface of the initial design.

**Table 1.** Materials property of the cam and electric contacts.

	Cam	Movable/Fixed Contact
Material type	Carbon steel (S45C)	Cu-Cr alloy
Density	$7.865 \times 10^{-6}$ kg/mm <sup>3</sup>	$8.96 \times 10^{-6}$ kg/mm <sup>3</sup>
Young's modulus	210 GPa	110.316 GPa
Allowable compressive yielding stress	2070 MPa	–
Ultimate tensile stress	2070 MPa	–
Brinell Hardness, H <sub>B</sub>	705	–
Poisson's ratio	0.30	0.34

### 3. Multibody Dynamic Analysis by MSC-ADAMS

To elucidate the dynamic characteristics of the cam-linkage composite operating mechanism of a VCB, a three-dimensional (3D) solid model was constructed using SolidWorks software (Figure 21). The model was then converted to the .x\_t format and imported into MSC-ADAMS software (Figure 22) to perform multibody dynamic analysis and simulation of the VCB operating mechanism.

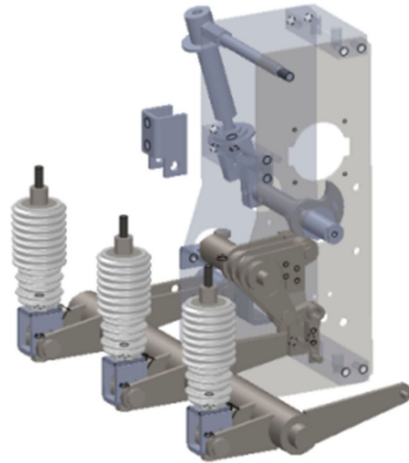


Figure 21. 3D solid model of the VCB operating mechanism.

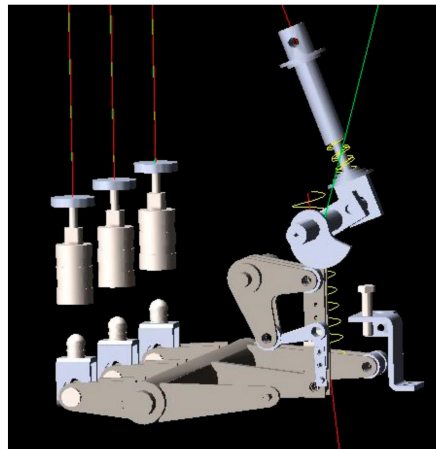


Figure 22. Simulation of the VCB mechanism by ADAMS.

#### 3.1. Simulation Setting

Before the kinematic and dynamic analyses of the VCB mechanism were performed, various parameters including the material characteristics of various bodies, joint types connecting the various links, elastic coefficients and amount of pre-compression/pre-stretching of the springs were given, as listed in Tables 1 and 2. As displayed in Table 1, both the compressive yielding stress and ultimate tensile stress of carbon steel S45C, which was subjected to heat treatment, including quenching and tempering at 27 °C, were equal to 2070 MPa [26]. The parameters of contact conditions between the cam and roller, and the movable/fixed contacts are listed in Table 3. Finally, the free-contact force was selected according to the simulation interval using the MSC-ADAMS/Solver Command function (Table 4).

**Table 2.** Parameters and pre-deformed amount of the springs.

	Elastic Coefficient of Spring (N/mm)	Pre-Compressed/Pre-Stretched (mm)	State of VCB
Closing springs	$k_{c1} = 7.72$	140 (compressed)	Opened state
	$k_{c2} = 9.33$	100 (compressed)	
Opening spring	$k_o = 16.6$	33.6 (stretched)	Closed state
Contact spring	$k_w = 82.4$	17 (compressed)	Closed state

**Table 3.** Parameters of contact conditions in ADAMS.

	Cam	Movable/Fixed Contact
Normal force		Impact
Stiffness		$10^5$
Force exponent	2.2	1.6
Damping	10	$10^3$
Penetration depth		0.1 (mm)

**Table 4.** Setting of simulation time and free-contact force.

	Simulation Time (s)	Steps	Free-Contact Force	State of VCB
I	0.0000~0.0032	100	deactivate	closed
II	0.0032~0.0278	300	activate	opened
III	0.0278~0.0450	500	deactivate	closed

### 3.2. Multibody Dynamic Analysis

The initial default setting for multibody dynamic analysis of the VCB operating mechanism was the closed state (Figure 2). The selected simulation time, free-contact force and state of the VCB are listed in Table 4.

Figures 23–25 illustrate the results of kinematic analysis and dynamic simulation of the initial VCB mechanism design using MSC-ADAMS. The results indicated the angular displacement of the cam, the displacement of the insulated rod, and the velocities of the movable contact and insulated rod. During 0–0.0032 s, the opening spring, contact spring, and closing springs simultaneously released energy from the initial closed state. The movable contact and fixed contact separate at approximately 0.0032 s, and the opening state of the VCB is initiated. During 0.0032–0.007 s, the insulated rod and movable contact simultaneously shifted downwards, and the open circuit process was completed at 0.007 s. Concurrently, the closing springs continued to release energy. At approximately 0.0131 s, the cam contacted with the roller, exerting a downward force on the roller and actuating the insulated rod and movable contact to synchronously shift upward. At 0.0278 s, the movable contact abruptly collided with the fixed contact, thereby the velocity of the movable contact sharply decreased to zero. The insulated rod continued to move upward with an abrupt decrease in velocity, thus compressing the contact spring in the VI. The closed state was completed at approximately 0.045 s. The overall rotation of the cam from the opened state to the closed states was  $140.6^\circ$ , with a contact stroke of 11 mm and the overall displacement of the insulated rod was 18 mm. The simulation results indicated that the average opening velocity of the movable contact was approximately 2.5 m/s, and the average closing velocity was approximately 1.71 m/s. These results indicated that the surplus work of the VCB operating mechanism system resulted in an excessively high closing velocity of the movable contact. Furthermore, the general output force simulated using MSC-ADAMS is

illustrated in Figure 17 (blue solid line) compared with those simulated using MATLAB-coded program (blue dashed line). The values were approximated and the curve trends were consistent in both curves. The main factor causing the differences is the quasi-static assumption in this work.

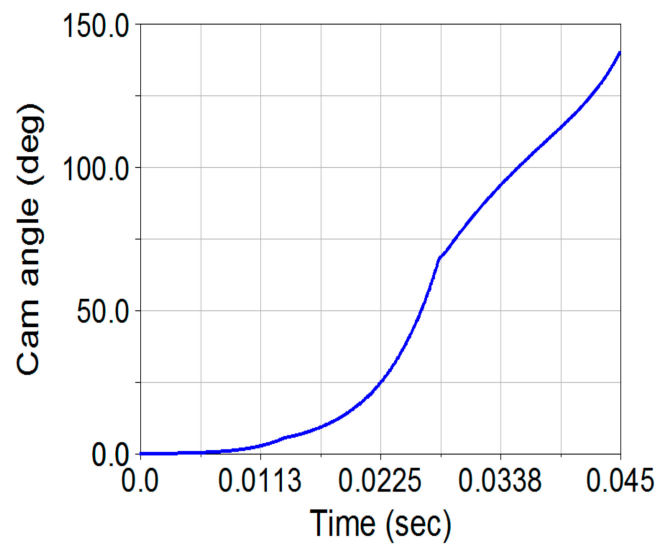


Figure 23. Angular displacement of the cam motion.

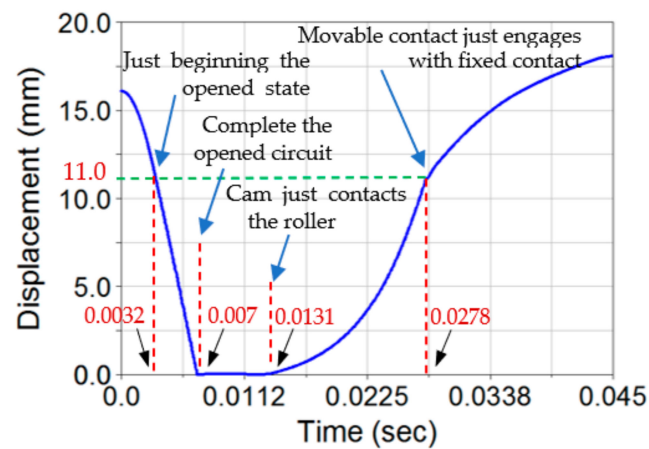


Figure 24. Displacement of the insulated rod.

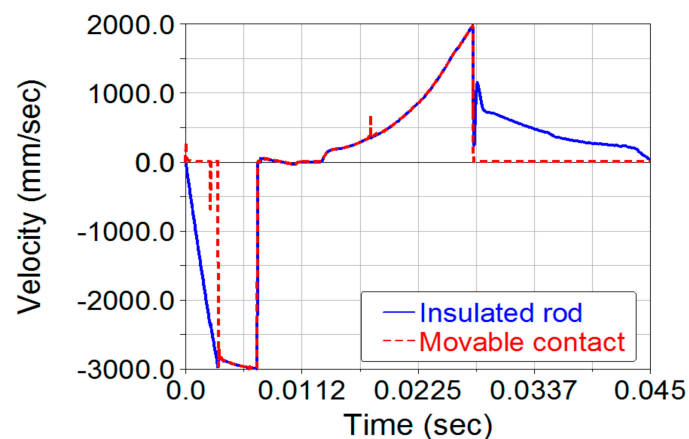


Figure 25. Velocities of the movable contact and insulated rod.

## 4. Optimal Design of the VCB Operation Mechanism

### 4.1. Differential Evolution Algorithm

Storn and Price [15] proposed the differential evolution (DE) algorithm, which is a well-known metaheuristic optimization algorithm that can be used to search for a global optimum solution in a D-dimension real variable space. The standard DE algorithm involves four basic steps: initialization, mutation, recommendation or crossover, and selection. Only the last three steps are repeated in subsequent DE iterations.

#### (1) Initialization

In the D-dimension real variable space, each vector, known as the genome/chromosome, forms a candidate solution of the optimization problem. The  $i$ -th parameter vector of the population at the current iteration ( $t$ ) can be expressed as follows:

$$\mathbf{x}_i^{(t)} = [x_{i,1}^{(t)}, x_{i,2}^{(t)}, \dots, x_{i,D}^{(t)}] \quad (32)$$

The initial populations ( $t = 1$ ) covered the entire parameter space as much as possible through uniform random distribution within a range constrained by the prescribed minimum and maximum bounds.  $\mathbf{x}_{\min} = [x_{\min,1}, x_{\min,2}, \dots, x_{\min,D}]$  and  $\mathbf{x}_{\max} = [x_{\max,1}, x_{\max,2}, \dots, x_{\max,D}]$ . Therefore, the  $j$ -th component of the  $i$ -th vector can be initialized as follows:

$$x_{i,j}^{(1)} = x_{\min,j} + \text{rand}_{i,j}(0, 1) (x_{\max,j} - x_{\min,j}) \quad (i = 1, 2, \dots, Np; j = 1, 2, \dots, D) \quad (33)$$

where  $\text{rand}_{i,j}(0, 1)$  is a uniformly distributed random number within the interval  $[0, 1]$ .  $Np$  denotes the number of populations,  $i$  denotes the index of solution vector, and  $j$  denotes the index of the parameter in the vector.

#### (2) Mutation

After initialization, a donor/mutant vector  $\mathbf{v}_i^{(t)}$  corresponding to each target vector  $\mathbf{x}_i^{(t)}$  in the current iteration ( $t$ ) was obtained according to outcome of the mutation operation. Figure 26 illustrates a simple DE mutation scheme ( $DE/rand/1$ ) in the 2D parametric space. The five most frequently used mutation strategies are listed below:

$$\begin{aligned} & DE/rand/1 : \\ & \mathbf{v}_i^{(t)} = \mathbf{x}_{r_1}^{(t)} + F(\mathbf{x}_{r_2}^{(t)} - \mathbf{x}_{r_3}^{(t)}) \\ & DE/rand/2 : \\ & \mathbf{v}_i^{(t)} = \mathbf{x}_{r_1}^{(t)} + F(\mathbf{x}_{r_2}^{(t)} - \mathbf{x}_{r_3}^{(t)}) + F(\mathbf{x}_{r_4}^{(t)} - \mathbf{x}_{r_5}^{(t)}) \\ & DE/best/1 : \\ & \mathbf{v}_i^{(t)} = \mathbf{x}_{best}^{(t)} + F(\mathbf{x}_{r_1}^{(t)} - \mathbf{x}_{r_2}^{(t)}) \\ & DE/best/2 : \\ & \mathbf{v}_i^{(t)} = \mathbf{x}_{best}^{(t)} + F(\mathbf{x}_{r_1}^{(t)} - \mathbf{x}_{r_2}^{(t)}) + F(\mathbf{x}_{r_3}^{(t)} - \mathbf{x}_{r_4}^{(t)}) \\ & DE/rand-to-best/1 : \\ & \mathbf{v}_i^{(t)} = \mathbf{x}_i^{(t)} + K(\mathbf{x}_{best}^{(t)} - \mathbf{x}_i^{(t)}) + F(\mathbf{x}_{r_1}^{(t)} - \mathbf{x}_{r_2}^{(t)}) \end{aligned} \quad (34)$$

The indices  $r_1, r_2, r_3, r_4$  and  $r_5$  are randomly generated within the range  $[1, Np]$  and  $r_1 \neq r_2 \neq r_3 \neq r_4 \neq r_5 \neq r_i$ .  $\mathbf{x}_{best}^{(t)}$  denotes the best individual vector with the best fitness function in the population at iteration  $t$ .  $\mathbf{x}_{r_2} - \mathbf{x}_{r_3}$  represents the difference vector; the mutation weighting factor (scale factor)  $F$  is a positive control parameter used to scale the difference vector and is usually selected within  $[0.4, 0.99]$ .

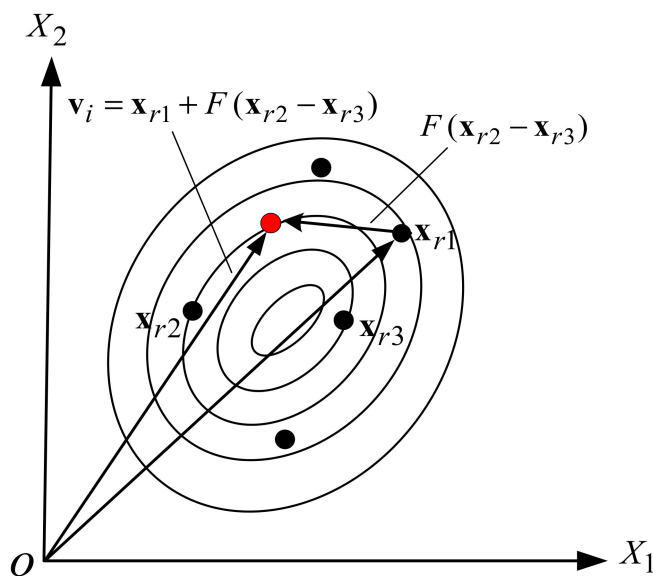


Figure 26. A simple DE mutation scheme in 2D parametric space.

(3) Crossover

Through uniform (or binomial) crossover, the components of the donor vector were combined with those of the target (parent) vector  $x_i^{(t)}$  to form a trail (offspring) vector

$$u_{i,j}^{(t)} = \begin{cases} u_{i,j}^{(t)} & \text{if } rand_{i,j}(0, 1) \leq CR \text{ or } i = i_r \\ v_{i,j}^{(t)} & \text{otherwise} \end{cases} \tag{35}$$

where  $CR$  is a pre-defined control parameter called the crossover rate, which ranges within  $[0, 1]$ .  $rand_{i,j}(0, 1)$  denotes a uniform random number within the range  $[0, 1]$  and ensures that the trail vector  $u_i^{(t)}$  includes at least one component from the donor vector  $v_i^{(t)}$ . Element  $i_r$  is a randomly selected integer from the set  $[1, 2, \dots, D]$ .

(4) Selection

Selection determines whether the target vector or the trial vector survives in the next iteration through the comparison of the corresponding objective function value.

$$x_i^{(t+1)} = \begin{cases} u_i^{(t)} & \text{if } f(u_i^{(t)}) \leq f(x_i^{(t)}) \\ x_i^{(t)} & \text{otherwise.} \end{cases} \tag{36}$$

where  $f(\cdot)$  is the objective function to be minimized.

Figure 27 illustrates the flow of the DE optimization algorithm. The optimal solution of a design problem is obtained through an iterative process to determine the fitness value of the candidate solutions; the favorable solutions are retained and unfavorable solutions are discarded until the optimal solution is determined. The advantages of the DE algorithm are its simple structure, easy implementation, and ability to achieve rapid convergence.

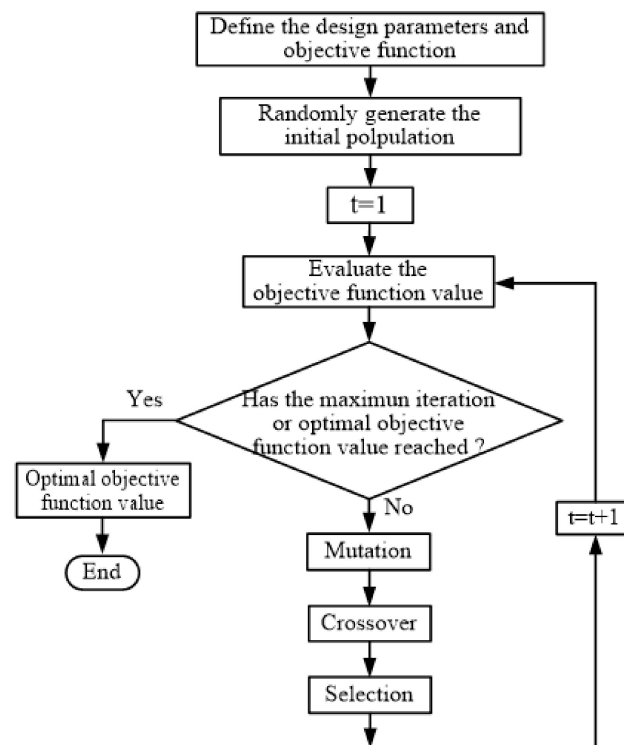


Figure 27. Flow chart of the DE optimization algorithm.

#### 4.2. Optimum Design of Cam Profile and Stiffness of Closing Springs

To improve the output force characteristics and reduce the characteristic forces of the VCB operating mechanisms, this study adopted the overall difference between the general output force and the general resistant force of the VCB operating mechanism as the objective function. Subsequently, the DE algorithm was employed to optimize the design problem. The optimal design of the VCB operating mechanism was achieved through two steps, the first step involved the optimal design of the cam profile and elastic coefficients of the two closing springs, which was first performed at this section, and the second step involved the optimal dimensional synthesis of the planar four-bar linkage.

##### (1) Design variables

The design variables include the coefficients  $(a_1, a_2, a_3)$  of the three-order polynomial angular displacement function of the oscillating roller follower and the spring stiffness  $(k_{c1}, k_{c2})$  of the two closing springs, the design variables can be expressed as a vector  $\mathbf{X}$ .

$$\mathbf{X} = [x_1, x_2, x_3, x_4, x_5]^T = [a_1, a_2, a_3, k_{c1}, k_{c2}]^T \quad (37)$$

The range of the design parameters were as follows:

$$\begin{aligned} 0 \leq x_1 \leq 0.5, \quad 0 \leq x_2 \leq 0.5, \quad -0.5 \leq x_3 \leq 0 \\ 4 \leq x_4 \leq 7.7, \quad 6 \leq x_5 \leq 9.3 \text{ unit of } x_4, x_5 \text{ (kN/m)} \end{aligned} \quad (38)$$

##### (2) Objective function

The optimum design the VCB mechanism is aimed to minimize the surplus work in the VCB mechanism during the closing operation. Therefore, according to Equation (26), the objective function was minimized as follows:

$$\text{Min}f(\mathbf{X}) = \sum_{i=1}^{N_s} \left| F_{oi} - \frac{F_{ri}}{\varepsilon} \right| + Mh(\mathbf{X}) \quad (39)$$

where  $F_o^i$ ,  $F_r^i$  represent the general output force and general resistant force of the mechanism at the  $i$ -th selected angular position of the cam;  $N_s$  represents the number of selected angular positions ( $N_s = 140$ ) of the cam during the closing stroke which the cam makes contact with the follower;  $h(\mathbf{X})$  denotes the penalty function; and  $M$  is an extremely high number ( $M = 10^6$ ).

### (3) Constraints

The specified contact stroke of the movable contact,  $s_c$ , was  $11 \pm 2$  mm, and the maximum angular displacement ( $\phi_{\max}$ ) of the follower link of the cam mechanism was constrained within the interval  $23^\circ \leq \phi_{\max} \leq 26^\circ$ . The constraint can be expressed as follows:

$$h(\mathbf{X}) : 23^\circ \leq \phi_{\max} \leq 26^\circ \quad (40)$$

### (4) Optimal design results

Table 5 displays the parameter settings for the optimal VCB mechanism design. This study employed the DE-gr method, which involved using a specified proportion of the crossover rate to the mutation factor, referred to as a golden ratio (0.618:0.382) [19]. Twenty-five numerical experiments were performed to obtain the best optimal solution, and each experiment had 300 generations. Table 6 lists the optimal results, indicating that the minimum value of objective function was  $1.74 \times 10^{-7}$ . Figure 28 displays the convergence rate of the optimization process, which rapidly converged to the optimal value in the 43rd generation. Figures 29 and 30 illustrate the dynamic analyses of the optimal VCB mechanism during the closing operation, performed using a MATLAB-coded program. Figure 29 displays the optimal cam profile and pitch curve (only actuated portion). The angular displacement curve of the oscillating follower of the optimal cam mechanism is illustrated in Figure 11 (blue solid line), it was identical to the specified motion curve displayed in Figure 4. The radius of curvature of the optimal cam profile is illustrated in Figure 13 (blue solid line). Figure 30a displays the normal contact forces (blue solid line) on the surface of the cam, Figure 30b displays the maximum Hertz contact stress (blue solid line) on surface of the cam, Figure 30c depicts the maximum shear stress (blue solid line) beneath the cam surface. The maximum Hertz contact stress and maximum shear stress in the DE-gr optimal design cam mechanism decreased considerably relative to those in the initial design. Notably, the highest Hertz contact stress and shear stress occurred at a cam rotation angle of  $140^\circ$  when the closing operation was completed. The shear yielding stress ( $\tau_y$ ) of the carbon steel (S45C) was  $\tau_y = 0.577\sigma_y = 1194$  MPa. Thus, the maximum Hertz contact stress and maximum shearing stress on and beneath the optimized cam surface were lower than the contact endurance stress and yielding shear stress, respectively (see Table 1). Figure 31 illustrates the analyses of the characteristic force of the optimal VCB mechanism during closing operation. The solid blue line represents the general output force, and the area under curve (AUC) of the general output force (meaning driving work) was slightly larger than the AUC of the general resistant force (meaning resistant work) of the VCB operating mechanism. The minimum surplus work can result in a decrease in an excessively high closing velocity of the movable contact. As illustrated in Figure 31, before the electric contacts collided with the fixed contact at  $s_1 = 11$  mm, the general output force was higher than the general resistant force, thereby facilitating closing operation. At  $s_1 > 11$  mm the general resistant force was abruptly higher than the general output force until the closing stroke was completed. Figure 32 displays the velocity of the movable contact simulated using MSC-ADAMS. The average closing velocity was 1.17 m/s, which was lower than 1.71 m/s in the initial VCB mechanism design; the obtained average closing velocity was nearly consistent with the required average closing velocity ( $0.9 \pm 0.2$  m/s). These results of analyses indicated that the optimal design of the cam profile and closing springs achieved in this study was feasible, and the DE-gr method was effective for optimizing the VCB operating mechanism.



**Table 5.** Parameters setting for DE-gr optimal design of cam profile and closing springs.

	DE-Gr Algorithm
Population number	100
Iteration number	300
Crossover method	Multiple point
Crossover rate	0.618
Mutation method	DE/best/1
Mutation factor	0.382
Selection	Tournament

**Table 6.** Optimal results of the cam profile and closing springs design.

Design Parameters	Initial Design	DE-Gr Optimization
$a_1$	0.240347	0.238432
$a_2$	0.011694	0.000226
$a_3$	-0.017243	-0.011492
$k_{c1}$ (N/mm)	7.720000	9.315336
$k_{c2}$ (N/mm)	9.330000	7.788183
Value of objective fun.	$1.75 \times 10^3$	$1.74 \times 10^{-7}$

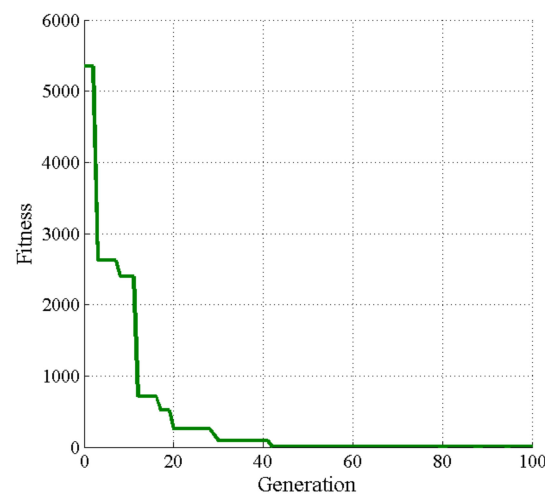


**Figure 28.** Convergence rate for DE-gr optimization of the cam profile and closing springs.

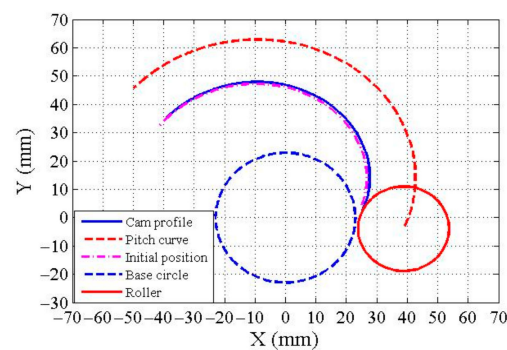
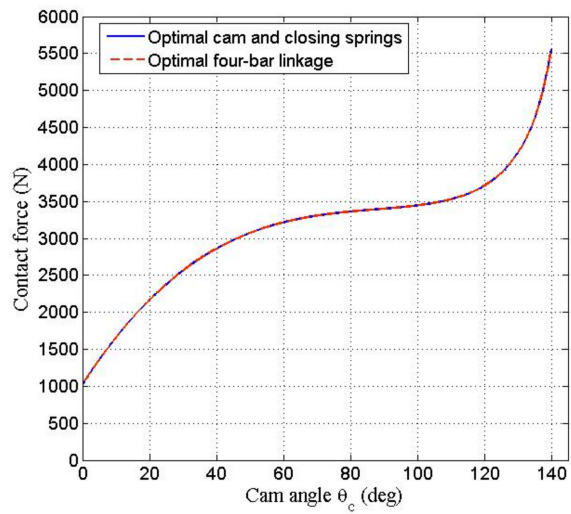
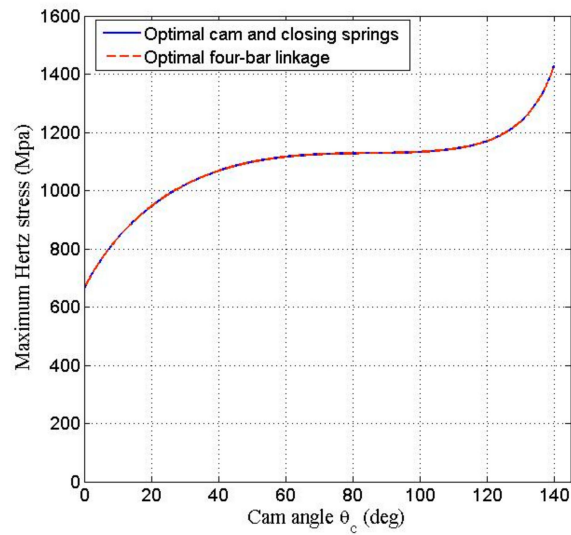


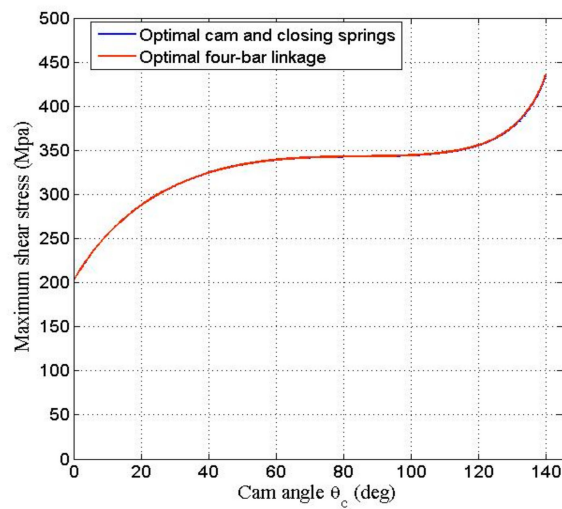
**Figure 29.** Optimal cam profile and pitch curve (only actuated portion).



(a) Normal contact force on surface of cam profile



(b) Maximum Hertz stress on cam surface for optimal cam design and four-bar linkage design



(c) Maximum shear stress beneath the cam profile

**Figure 30.** Normal contact force, Hertz stress, and maximum shear stress for the optimal VCB operating mechanism.

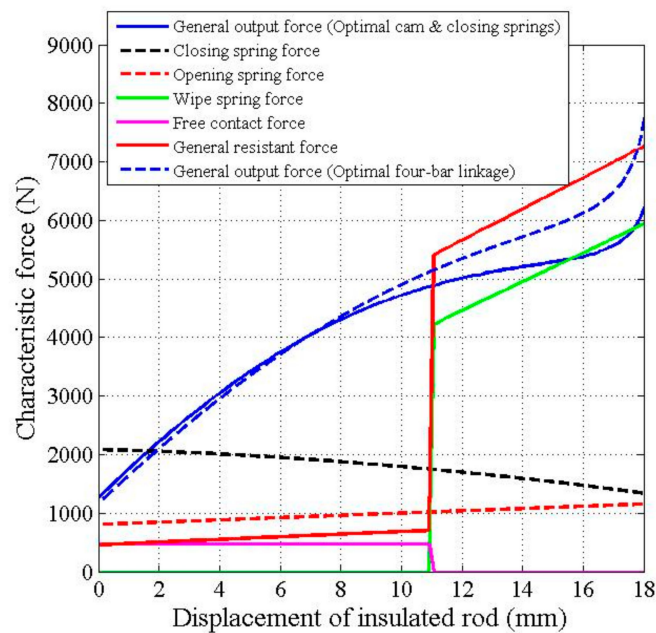


Figure 31. Characteristic forces of the optimal VCB mechanisms.

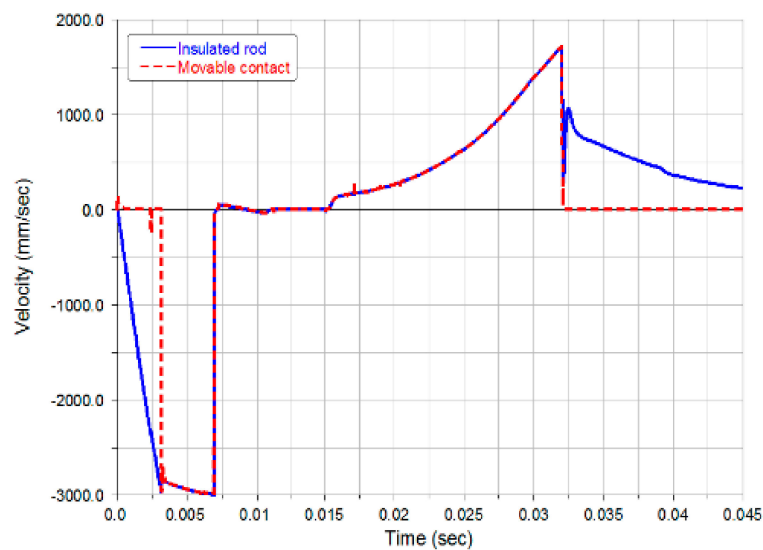


Figure 32. Velocity of movable contact and insulated rod during closing process (Simulated by MSC-ADAMS).

#### 4.3. Optimal Synthesis of the Four-Bar Linkage

The second step of the optimal VCB operating mechanism design involved the optimal dimensional synthesis of the four-bar linkage. It was conducted based on the optimal design of the cam profile and closing springs obtained in previous step. The parameters of the DE-gr algorithm, minimum objective function, and experiment number were the same as those used in the first step of the optimal design.

##### (1) Design variables

The dimensions of the four-bar linkage (Figures 6 and 9), except for the length of the input link 2, the length of lever EM ( $\ell_5$ ) and the setting angle of the fixed link were used as the design variables that were expressed as a vector  $\mathbf{X}$ .

$$\mathbf{X} = [x_1, x_2, x_3, x_4, x_5]^T = [\ell_1, \ell_3, \ell_4, \ell_5, \theta_1]^T \tag{41}$$

The range of the design variables of the four-bar linkage were as follows:

$$\begin{aligned} 70 \leq x_1 \leq 150, \quad 70 \leq x_2 \leq 150, \quad 70 \leq x_3 \leq 150 \\ 50 \leq x_4 \leq 100, \quad -\pi \leq x_5 \leq -0.5\pi \end{aligned} \quad (42)$$

(2) Objective function

The objective function was expressed as Equation (39).

(3) Constraints

The four-bar linkage was constrained by the conditions of the Grashoff mechanism [21] such that the length of the links satisfied the following requirement:

$$h(\mathbf{X}) : r_s + r_l < r_p + r_q \quad (43)$$

where  $r_s$ ,  $r_l$  represented the lengths of the shortest link and largest link, respectively, and  $r_p$ ,  $r_q$  were the lengths of the other two links.

(4) Optimal design results

Table 7 lists the results of optimal design of the four-bar linkage; the value of the objective function was  $7.13 \times 10^{-10}$  (approximately zero). Figure 33 displays the convergence rate of the optimization of the four-bar linkage, the value rapidly converged to the optimal value in the 18th generation. The output–input curve of the optimal four-bar linkage is displayed in Figure 15 (blue solid line). The results indicated that the motion range,  $[-6, 6]$ , of the output link of optimal four-bar linkage was more symmetric than that of the initial design,  $[-8, 4]$  (Figure 15, red dashed line), indicating that the optimization more satisfied the assumed conditions of Equations (1) and (4) and the specified motion curve shown in Figure 4. Figure 30 (shown by red dashed lines) displays the normal contact force (Figure 30a), the Hertz contact stress (Figure 30b) and maximum shear stress (Figure 30c) on and beneath the cam surface due to the optimized four-bar linkage. Obviously, the curves of normal contact force, Hertz contact stress and maximum shear stress shown in Figure 15 were consistent each other in both optimal designs. These results of stress analyses revealed that both the optimal designs were feasible. The general output force generated during the closing operation in the optimal four-bar linkage design is displayed in Figure 31 by a blue dashed line. Figure 34 indicates the comparison of the driving work (AUC of the general output force) and general resistant work (AUC of the general resistant force) among the various VCB operating mechanism designs, namely initial design, optimum design of the cam and closing springs, and optimum design of the four-bar linkage. The results of dynamic analyses of the optimal VCB mechanism in the second step revealed that they were slightly different from those of the optimum VCB mechanism with the optimal cam and closing springs in the first step. This indicates that both of the two optimal VCB mechanism designs are safe and feasible solutions, and the optimal four-bar linkage can serve as an alternative choice to replace the initial four-bar linkage while considering the layout of the VCB mechanism.

**Table 7.** Optimal design of the four-bar linkage.

	Initial Design	DE-Gr Optimization
$l_1$	139.790000	117.263920
$l_3$	124.700000	99.825118
$l_4$	140.000000	133.857634
$l_5$	90.000000	85.046620
$\theta_1$	$-121.980^\circ$	$-123.967^\circ$
Obj. function value	$1.74 \times 10^{-7}$	$7.13 \times 10^{-10}$

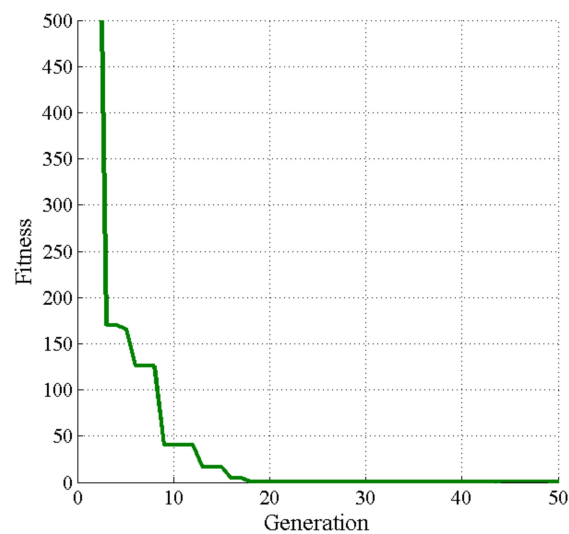


Figure 33. Convergence rate of the optimization of the four-bar linkage.

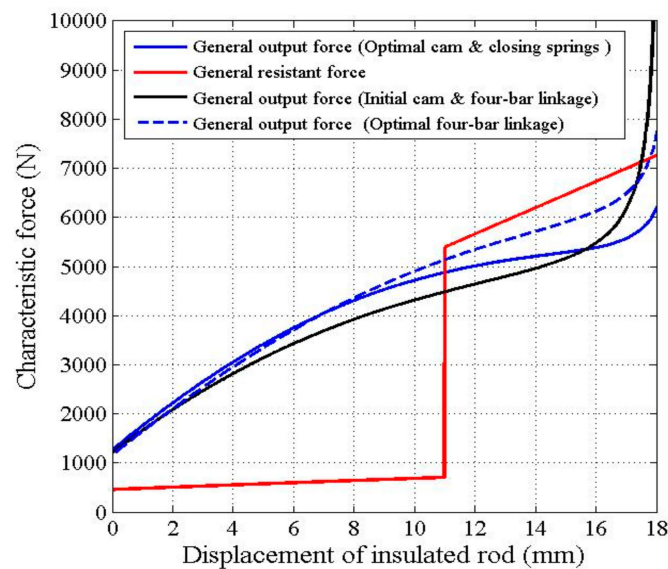


Figure 34. Comparison of the output work and resistant work among different VCB mechanisms designs.

## 5. Conclusions

This paper proposes a method which combines the analytical method and optimization approach for designing a spring-actuated cam-linkage operating mechanism used in a 12 kV, 25 kA VCB. The designed cam profile was based on three-order polynomial motion curve of the follower according to the specified motion of the VCB mechanism. The sum of differences between the general output force and the general resistant force of the VCB operating mechanism during the closing operation was adopted as the objective function to be minimized. Further, a DE-gr algorithm (that incorporated a golden ratio (0.618:0.382) as the ratio of crossover rate to mutation factor) was employed to optimize the design of the cam profile and elastic coefficients of closing springs, and then to optimize the design of the four-bar linkage. The dynamic analyses of the characteristic forces and the contact stress analyses of the optimal VCB operating mechanism were performed using a MATLAB-coded program. The kinematic simulation and the results of dynamic analyses were validated using the multibody dynamic software MSC-ADAMS. The optimal results revealed that the surplus output work in the initial VCB operating mechanism was effectively minimized to zero in the optimal VCB operating mechanism. Thus, the average closing velocity of the

movable contact was considerably reduced, and the maximum Hertz contact stress and maximum shear stress on and beneath the cam surface were significantly decreased. The proposed optimal design of the VCB operation mechanism helps to prevent an excessive increase in the average closing velocity of the movable contact in the VI.

**Author Contributions:** Y.-H.K.: Conceptualization, methodology, validation, investigation, resources, writing-original draft preparation, writing-review and editing, supervision. H.-C.H.: Investigation, writing-review and editing. B.-Y.Y.: Software, data curation, validation, formal analysis. All authors have read and agreed to the published version of the manuscript.

**Funding:** This research was funded by Taiwan Calsonic Co., Ltd.

**Informed Consent Statement:** Not applicable.

**Data Availability Statement:** Not applicable.

**Acknowledgments:** The authors would like to thank the research fund supported from Taiwan Calsonic Co., Ltd. and the valuable opinions suggested by vice-president Fan-Ming Li, and manager Chih-Chen Chang.

**Conflicts of Interest:** The authors declare no conflict of interest.

## References

1. Flurscheim, C.H. *Power Circuit Breaker Theory and Design, Revised ed.*; Peter Peregrinus Ltd.: London, UK, 1985.
2. Ahn, G.Y.; Jeong, K.Y. Optimization of the spring design parameters of a circuit breaker to specify the specified dynamic characteristics. *Int. J. Precis. Eng. Manuf.* **2004**, *5*, 43–49.
3. Ahn, K.Y.; Kim, S.H. Modelling and analysis of a high-speed circuit breaker mechanism with a spring-actuated cam. *Proc. Inst. Mech. Eng. Part C J. Mech. Eng. Sci.* **2001**, *215*, 663–672. [[CrossRef](#)]
4. Pisano, A.P.; Freudenstein, F. An experimental and analytical investigation of the dynamic response of a high-speed cam follower system, Part 1: Experimental investigation. *ASME J. Mech. Transm. Autom. Des.* **1983**, *105*, 692–698. [[CrossRef](#)]
5. Pisano, A.P.; Freudenstein, F. An experimental and analytical investigation of the dynamic response of a high-speed cam-follower system. Part 2: A combined, lumped/distributed parameter dynamic model. *ASME J. Mech. Transm. Autom. Des.* **1983**, *105*, 699–704. [[CrossRef](#)]
6. Root, R.R.; Ragsdell, K.M. The circuit breaker—a practical example in engineering optimization. *Mech. Mach. Theory* **1983**, *18*, 229–235. [[CrossRef](#)]
7. Jobes, C.C.; Palmer, G.M.; Means, K.H. Synthesis of a controllable circuit breaker mechanism. *ASME J. Mech. Des.* **1990**, *112*, 324–330. [[CrossRef](#)]
8. Kim, J.H.; Ahn, K.Y.; Kim, S.H. Optimal synthesis of a spring-actuated cam mechanism using a cubic spline. *Proc. Inst. Mech. Eng. Part C J. Mech. Eng. Sci.* **2002**, *216*, 875–883. [[CrossRef](#)]
9. Chen, F.C.; Tzeng, Y.F. On the dynamics of a spring-type operating mechanism for a gas-insulated circuit breaker in open operation using the Lagrange equation. *Proc. Inst. Mech. Eng. Part C J. Mech. Eng. Sci.* **2002**, *216*, 831–843. [[CrossRef](#)]
10. Chen, F.C. On the design of spring-actuated mechanism for 69KV SF6 gas insulated breaker. *ASME J. Mech. Des.* **2003**, *125*, 840–845. [[CrossRef](#)]
11. Yoo, W.S.; Kim, S.O.; Sohn, J.H. Dynamic analysis and Design of a high voltage circuit breaker with spring operating mechanism. *J. Mech. Sci. Technol.* **2007**, *21*, 2101–2107. [[CrossRef](#)]
12. Yu, M.J.; Wang, L.C.; Huang, S.C. Optimal dimensional synthesis of the trigger mechanism of a high-voltage circuit breaker. *J. Chin. Inst. Eng.* **2013**, *36*, 146–156. [[CrossRef](#)]
13. Jang, J.S.; Yoon, C.G.; Ryu, C.Y.; Kim, H.W.; Bae, B.T.; Yoo, W.S. Optimization of the switch mechanism in a circuit breaker using MBD based simulation. *Sci. World J.* **2015**, *2015*, 347047. [[CrossRef](#)] [[PubMed](#)]
14. Liu, Y.Y.; Chen, D.G.; Yuan, H.W.; Ji, L.; Ma, Z. Research of dynamic optimization for the cam design structure of MCCB. *IEEE Trans. Compon. Packag. Manuf. Technol.* **2016**, *6*, 390–399. [[CrossRef](#)]
15. Storn, R.; Price, K. Differential evolution—a simple and efficient heuristic for global optimization over continuous spaces. *J. Glob. Optim.* **1997**, *11*, 341–359. [[CrossRef](#)]
16. Acharyya, S.K.; Mandal, M. Performance of EAs for four-bar linkage synthesis. *Mech. Mach. Theory* **2009**, *44*, 1784–1794. [[CrossRef](#)]
17. Lin, W.Y. A GA-DE hybrid evolutionary algorithm for path synthesis of four-bar linkage. *Mech. Mach. Theory* **2010**, *45*, 1096–1107. [[CrossRef](#)]
18. Ortiz, A.; Cabrera, J.A.; Nadal, F.; Bonilla, A. Dimensional synthesis of mechanisms using differential evolution with auto-adaptive control parameters. *Mech. Mach. Theory* **2013**, *64*, 210–229. [[CrossRef](#)]
19. Kang, Y.H.; Lin, J.W.; You, W.C. Comparative study on the synthesis of path-generating four-bar linkages using metaheuristic optimization algorithms. *Appl. Sci.* **2022**, *12*, 7368. [[CrossRef](#)]

20. Yu, L.; Geng, Y.S.; Liu, Z.Y.; Sun, L.Q.; Yao, J.J. Relationship between displacement characteristics of a 126KV vacuum circuit breaker and spring type operating mechanism. In Proceedings of the IEEE Conference 23rd Symposium on Discharges and Electrical Insulation in Vacuum, Bucharest, Romania, 15–19 September 2008; pp. 137–140.
21. Yan, H.S.; Wu, L.I. *Mechanisms*, 4th ed.; Tung Hua Books: Taipei City, Taiwan, 2014.
22. Timoshenko, S.P.; Gooder, J.P. *Theory of Elasticity*, 3rd ed.; McGraw-Hill: New York, NY, USA, 1973; pp. 403–419.
23. Budynas, R.G.; Nisbett, J.K. *Shigley's Mechanical Engineering Design*, 10th ed.; McGraw-Hill Education: New York, NY, USA, 2015; pp. 138–140.
24. Norton, R.L. *Cams Design and Manufacturing Handbook*; Industrial Press: New York, NY, USA, 2002.
25. Ugural, A.S.; Fenster, S.K. *Advanced Strength and Applied Elasticity*, 4th ed.; Pearson Education Taiwan Ltd.: New Taipei City, Taiwan, 2004.
26. Zhuang, M.G. *Mechanical Design and Analysis-Part II*; Fu-Win Book Company: Tainan City, Taiwan, 1990; pp. 1705–1706. (In Chinese)

**Disclaimer/Publisher's Note:** The statements, opinions and data contained in all publications are solely those of the individual author(s) and contributor(s) and not of MDPI and/or the editor(s). MDPI and/or the editor(s) disclaim responsibility for any injury to people or property resulting from any ideas, methods, instructions or products referred to in the content.